

# Analytical modeling of a cyclorotor in hovering state

Jakson A Leger<sup>1</sup>, José C Páscoa<sup>2</sup> and Carlos M Xisto<sup>3</sup>

Proc IMechE Part G:  
J Aerospace Engineering  
0(0) 1–15  
© IMechE 2015  
Reprints and permissions:  
sagepub.co.uk/journalsPermissions.nav  
DOI: 10.1177/0954410015569285  
uk.sagepub.com/jaero



## Abstract

In the paper it is proposed and described in detail a mathematical model that is able to assist in the design of cycloidal rotors. The method is formulated on a semi-empirical way including unsteady aerodynamic effects that are based on first principles. It is able to predict the overall generated thrust and the power required by the operation of the cycloidal rotor. The model also includes a kinematic package that can provide an instantaneous design and animation of the cycloidal rotor under different regimes of operation. For validation it was addressed three different rotor configurations where it was varied several rotor parameters, namely: pitch amplitude; pitching axis location; blade chord; airfoil thickness; phase angle of eccentricity. It was shown that the proposed model is able to provide a good estimation of thrust and power when compared with the experimental data from these different sources, showing that the semi-empirical approach could be applied in a more general way.

## Keywords

Cycloidal rotor, parametric study, analytical model

Date received: 9 April 2014; accepted: 21 December 2014

## Introduction

The EU-FP7 project cycloidal rotor optimized for propulsion (CROP) is conducting research on the development of cycloidal rotors for aeronautical propulsion. A cycloidal propeller is an aircraft propulsion system that is composed by several blades rotating about a horizontal axis perpendicular to the flight direction. Figures 1 and 2 show a 3-D representation of a cyclorotor configuration and an example of application for air-vehicles. The rotor blades prescribe a periodic change on their pitch angle over a cycle of rotation. Thus, the resulting kinematics of each blade is the combination of rotational and oscillating motions. This combined effect is obtained through the implementation of a blade pitching mechanism. This mechanical system can also change the oscillatory behavior, since for each position of the circle described by the rotor, i.e. azimuth angle  $\Psi$ , the blade pitch angle can be changed by varying the eccentricity phase angle  $\varepsilon$ , and the magnitude of eccentricity  $e$  (see Figure 3). This particular feature allows changes in the magnitude and direction of thrust (perpendicular to the rotating axis) almost instantly.<sup>1</sup> Therefore, the introduction of cycloidal propulsion systems into fixed wing, rotor fixed wing hybrid aircrafts<sup>2</sup> and micro-air-vehicles,<sup>3</sup> could improve the maneuverability of the aircrafts in vertical take-off and landing (VTOL), hover, and forward flight conditions. Due to the highlighted

characteristics, cycloidal blade systems have many applications. Research and development activities for mobile robots using cyclorotors have been also increasing in these recent years.<sup>4</sup> Experiments have been carried out to analyze cyclorotor applications for airships, aircrafts, navy vessels, and lighter-than-air vehicles. Thus, it has a strong potential for civilian and military applications.<sup>5–7</sup> The figure-of-merit is a parameter often used as efficiency metric for helicopter rotors and for the optimization study of flying wings.<sup>8</sup> In the case of cyclorotors, this parameter has also been used as a way of measuring efficiency. Several authors have performed research on the efficiency of cyclorotors.<sup>9–11</sup> Benedict et al.<sup>12</sup> studied the efficiency of cycloidal rotors and compared it to that of conventional rotors. He has also shown that the optimized cyclorotor has significantly higher power loading (thrust generated per unit of power)

<sup>1</sup>University of Beira Interior, Covilha, Portugal

<sup>2</sup>Departamento de Engenharia Electromecânica, Center for Mechanical and Aerospace Science and Technologies (C-MAST), Universidade da Beira Interior, Covilhã, Portugal

<sup>3</sup>Departamento de Engenharia Electromecânica, Universidade Beira Interior, Covilhã, Portugal

### Corresponding author:

Jakson A Leger, University of Beira Interior, Convento de Sto. António, Covilha 6201-001, Portugal.

Email: leger\_mec@hotmail.com

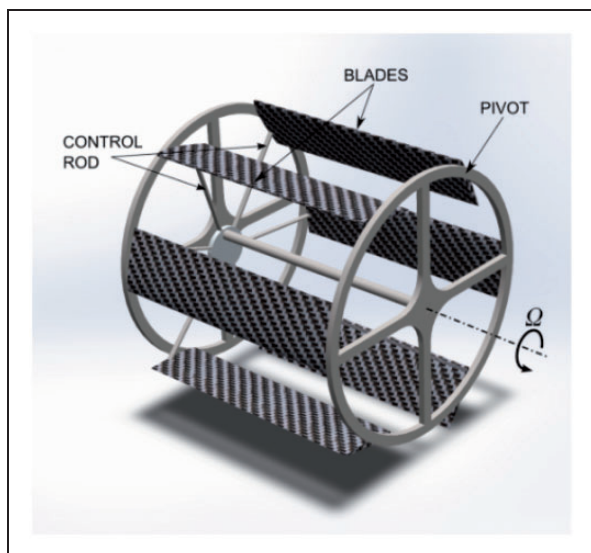


Figure 1. Three-dimensional representation of a cyclorotor.

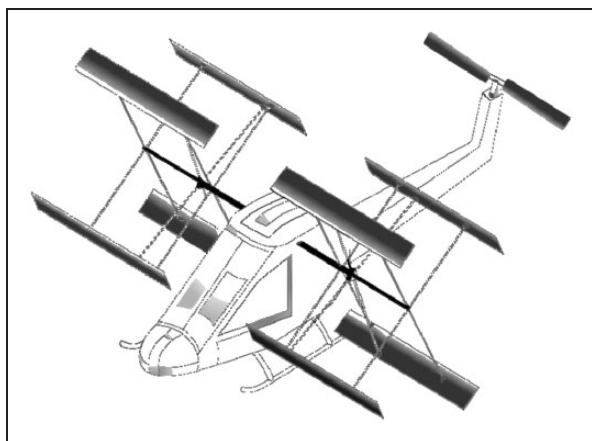


Figure 2. Possible air-vehicle operating with a cyclorotor.

compared to a conventional rotor when operating at the same disk loading (thrust generated per unit of cycloidal rotor rectangular projected area).<sup>13</sup> Nevertheless, its large rotating structure may result in a weight increase.<sup>14,15</sup> Many experimental studies and some computational fluid dynamics (CFD) computations have also been performed in order to analyze the generated thrust, and also the power required for hovering and forward flight conditions.<sup>16–19</sup> Through all these tests it was confirmed that thrust and power vary with the square and cube of rotational speed, respectively. In a flat plate airfoil, CFD simulations indicate that there are a leading edge and a trailing edge vortex shedding due to blade's dynamic stall.<sup>20</sup> The interaction between these shed vortices and the downstream blade can, under certain conditions, improve thrust generation due to a delay of stall.<sup>20</sup> However, aeroelastic analyses have shown that the blade torsion can cause a reduction in the blade aerodynamic efficiency, thus decreasing the thrust production capability of the cycloidal

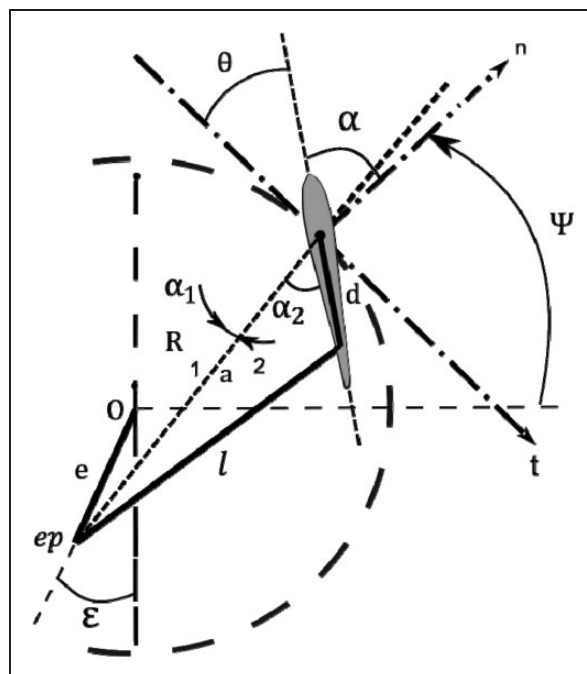


Figure 3. Pitch mechanic control system.

propeller.<sup>21</sup> This is due to the deformation caused by torsional moment created by the forces acting on the blades. In order to reduce the bending stress, carbon spars located at the front and rear inner blade positions have been used.<sup>15</sup> The aerodynamic effects are largely influenced by the blade oscillating motion, allowing exploitation of higher angles of attack without the occurrence of stall phenomenon. In order to analytically model the cyclorotor behavior the blade element theory and the stream tube model have regularly been used. In these models a control volume is defined, to which is applied the principle of mass, momentum, and energy conservation.<sup>22</sup> In such models the analysis is done at the pivot point. However, the points on the chord line have different rotating velocities. This speed variation along the chord unevenly influences the angle of attack, before and after the pivot point position. This feature is known as virtual camber effect and influences the attained thrust levels.<sup>23</sup> Thus, it may be stated that the blades are actually subjected to a curvilinear flow. The cascade effect in a cycloidal rotor analysis can initially be ignored due to the combined effect of low Reynolds number and low solidity values.<sup>24</sup> This flowfield behavior has recently been confirmed by experimental testing using particle image velocimetry (PIV).<sup>25</sup>

In following paper it is proposed a new semi-empirical model for predicting the thrust generated and power is required by the cycloidal rotor. The models are devised using an empirical parameter but includes first principles theory in order to account for the effects of unsteady aerodynamics. In the next section it is described the equations that rule the blade pitching mechanism. It is shown that a four-bar

linkage system cannot describe an ideal cycloidal motion due to a non-perfect intersection of each blade–chord perpendicular line. In “Oscillating blades motion kinematics” section the equations that describe the rotor kinematics are presented and analyzed in terms of rotational speed and eccentricity phase angle. In “The equivalent rotor model for parametric design of cycloidal rotors” section the proposed aerodynamic model is described in detail. It starts by presenting the equations that allow for the design and animation of the cycloidal rotor. Afterwards the dynamic part of the model that includes the unsteady aerodynamic effects and the derivation of the empirical parameter is addressed. “The equivalent rotor model for parametric design of cycloidal rotors” section ends by presenting the algorithm flowchart. In “Analytical model results” section, the proposed model is validated with experimental data from different sources.

## Mechanism and blade position control

Any analytical model that aims to compute thrust and power in cyclorotors should model, beforehand, each blade position and its pitch angle, since forces depend on the blade angle of attack which, in turn, depends on blade azimuthal location. Looking at Figure 3 the pitch angle is  $\theta = \frac{\pi}{2} - \alpha$  with  $\alpha = \alpha_1 + \alpha_2$ . By applying sine and cosine theorems to triangle 1, the distance from the pivot point to eccentricity point and angle  $\alpha_1$  can be easily obtained. Applying cosine theorem to triangle 2 the length of the control rod,  $l$ , is then related to angle  $\alpha_2$ . These can be expressed by equations,

$$a^2 = e^2 + R^2 - 2eR \cos\left(\Psi + \varepsilon + \frac{\pi}{2}\right) \quad (1)$$

$$\frac{\sin(\alpha_1)}{e} = \frac{\cos\left(\Psi + \varepsilon + \frac{\pi}{2}\right)}{a} \quad (2)$$

$$l^2 = a^2 + d^2 - 2ad \cos(\alpha_2) \quad (3)$$

By combining the previous expressions it can be easily concluded that the blade pitch angle complies in full with the following equation:

$$\theta = \frac{\pi}{2} - \sin^{-1}\left[\frac{e}{a} \cos(\Psi + \varepsilon)\right] - \cos^{-1}\left[\frac{(a^2 + d^2 - l^2)}{2ad}\right] \quad (4)$$

The position of a single blade is not enough to compute the overall sum of vertical and horizontal forces that are generated by the propeller in each instant. It is necessary to know all blade positions at a single instant. Assuming that one blade initial location is known,  $\Psi_1(0)$ , the others are easily obtained through arithmetic progression terms whose ratio is  $\frac{2\pi}{N}$ , shown in equation (5). Once the initial blade positions are known, their position at each instant

$\Psi(t) = \Psi_i(0) + \Omega t$  and also their inclination  $\theta(t) = f[\Psi(t)]$  are readily obtained,

$$\Psi_i(0) = \Psi_1(0) + \frac{(i-1)2\pi}{N} \quad (5)$$

## Analysis of cycloidal motion between mechanical and ideal cycloidal systems

To obtain a perfect cycloidal blade motion it is required that the perpendicular lines to the profile chords of each blade intersect at the same point (point B in Figure 4). This common point where the lines intersect is defined as steering center.<sup>26–29</sup> With the aim of analyzing the existence of a steering center for whatever may be the dimension of the mechanical pitch control system Figure 4 may be considered. In other words, it was searched for the blade pitch angle so that there is the steering center and then it was compared to the real pitch angle imposed by the mechanical system given by equation (4). Therefore, let us consider that the blade is at an azimuthal position  $\Psi$  oscillating around the pivot point A.

By analyzing the points in Figure 4, and their respective coordinates, vectors  $\vec{OA}$  and  $\vec{BA}$  can be defined. By resorting to pure analytical geometry the perpendicular vectors, to each one of them, can be found. These vectors are given by equations (6) and (7). Vector  $\vec{TA}$ , which is perpendicular to  $\vec{OA}$ , is the tangent vector to the circle described by the rotor. Assuming that point B is the steering center, then the slope of the perpendicular vector to vector  $\vec{BA}$ , i.e.  $\vec{PA}$ , can be used to find the blade slope  $\theta$  for each azimuth angle, so that the intersection point is unique. This is done by applying inner product to vectors  $\vec{TA}$  and  $\vec{PA}$ . However, for inner product, the pitch angle  $\theta$  has always the same value independent from the vector  $\vec{PA}$ , inside or outside of the circle described by the rotor. Actually, for each one of the cases, the

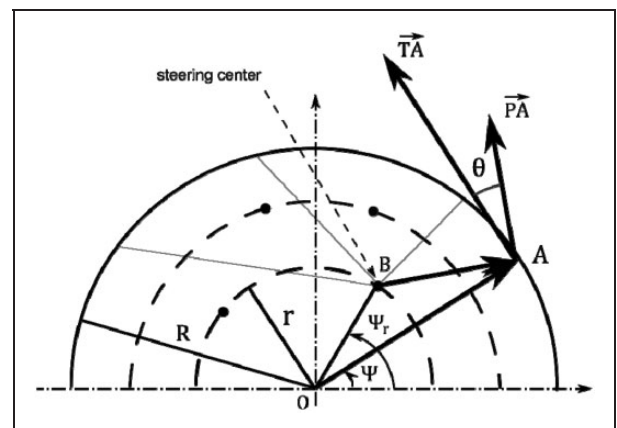


Figure 4. Steering point center analysis.

pitch angle has opposite signs, whose understanding is justified by the definition of the outer product. Thus, in order to obtain a steering center, the pitch angle must be entirely expressed by equation (8).

$$\vec{TA} = (-R \sin(\Psi), R \cos(\Psi)) \quad (6)$$

$$\vec{PA} = (-R \sin(\Psi) + r \sin(\Psi_r), R \cos(\Psi) - r \cos(\Psi_r)) \quad (7)$$

$$\theta = \frac{\vec{PA} \times \vec{TA}}{|\vec{PA} \times \vec{TA}|} \cdot \cos^{-1} \frac{\vec{PA} \cdot \vec{TA}}{|\vec{PA}| |\vec{TA}|} \quad (8)$$

The rotor defined in Table 1 is used to test equation (8). Here, equation (4) is used concurrently in order to counter check equation (8). Let us assume that the pivot point is at 25% from the leading edge, and that the considered phase angle of eccentricity is 45°. Yet, it must be carefully identified that the system axis, from which those equations were derived, are different. A phase angle of 45°, in the mechanical control system, relates to a 225° angle in the system defined by the steering center. The magnitude of the eccentricity is set so that one obtains the same maximum and minimum pitch angle in both cases. One can clearly see through Figure 5 the difference between the two pitch curves. Representing now the blades by their respective chords, Figures 6 and 7 can be generated using a pure mathematical model. Figure 6 shows the real slope of the blades imposed by the pitch mechanical system, that is to say, by using equation (4). However, Figure 7 comes up with the slope that the blades would have to assume so that the blades path is a pure cycloidal motion. As previously said, it is got by using equation (8). It is geometrically visible that for all possible dimensions, for the selected mechanical control system one cannot obtain a pure cycloidal motion.

### Oscillating blades motion kinematics

In order to include the aerodynamic effects, due to the oscillating motion, it is necessary to compute the

**Table 1.** Rotor parameter.

Variable	Value
Airfoil	NACA 0012
Rotor diameter (m)	1.2
Span (m)	1.2
Chord (m)	0.4
Number of blade	6
Length of control rod (m)	0.6055
Magnitude of eccentricity (m)	0.038
$d$ (m)	0.09
Maximum and minimum pitch angle (°)	25.2; -25.2

oscillating angular velocity  $\omega$  and angular acceleration acc. The pitch angle is a function of the azimuthal angle which, in turn, is a function of time. Equation (9) results from a simple chain rule application,

$$\omega = \frac{d\theta}{dt} = \frac{d\theta}{d\Psi} \cdot \frac{d\Psi}{dt} = \frac{d\theta}{d\Psi} \cdot \Omega \quad (9)$$

It was also defined  $\text{acc} = \frac{d\omega}{dt} = \frac{d\omega}{d\Psi} \cdot \frac{d\Psi}{dt} = \frac{d\omega}{d\Psi} \cdot \Omega$ . It is possible to compute  $\frac{d\omega}{d\Psi}$ , and consequently acc, as can be seen through

$$\frac{d\omega}{d\Psi} = \frac{d}{d\Psi} \left[ \frac{d\theta}{d\Psi} \cdot \Omega \right] = \Omega \cdot \frac{d}{d\Psi} \left( \frac{d\theta}{d\Psi} \right) = \Omega \cdot \frac{d^2\theta}{d\Psi^2} \quad (10)$$

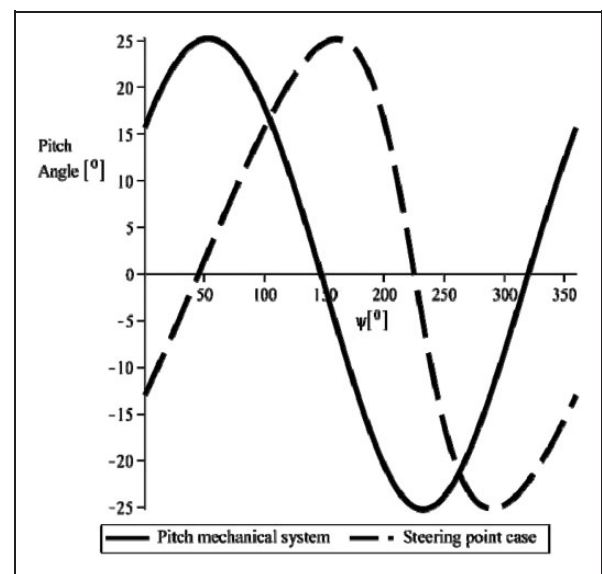


**Figure 5.** Pitch curves obtained in the mechanical control system axis and in the steering point axis system.

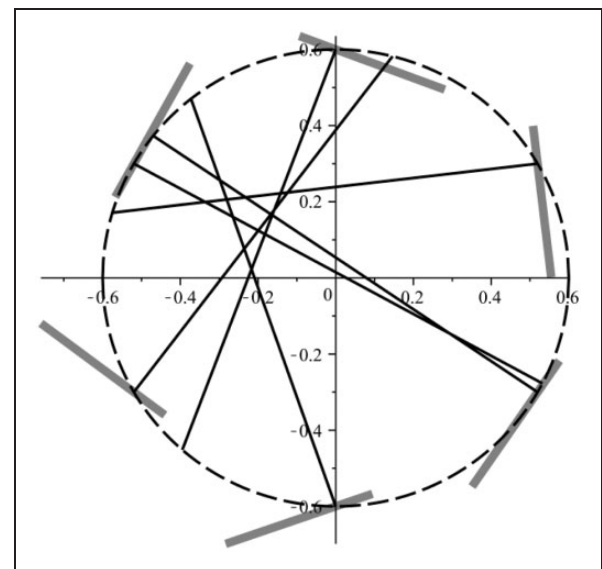


**Figure 6.** Geometric analysis of perpendicular lines, demonstrating the impossible definition of a pure cycloidal motion.



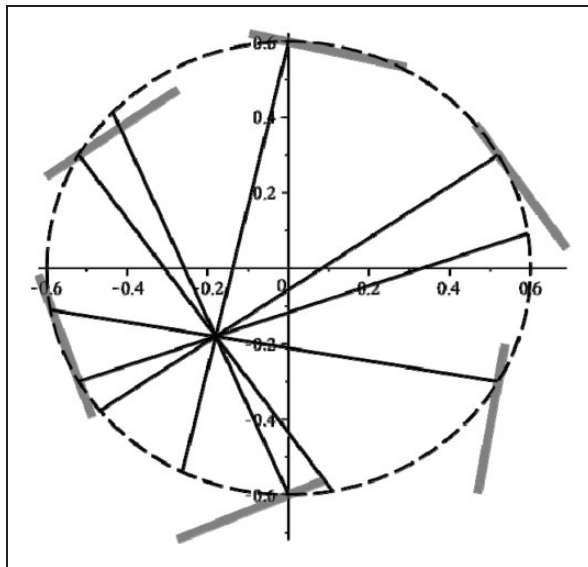


**Figure 7.** Geometric analysis of perpendicular lines, demonstrating a pure cycloidal motion.

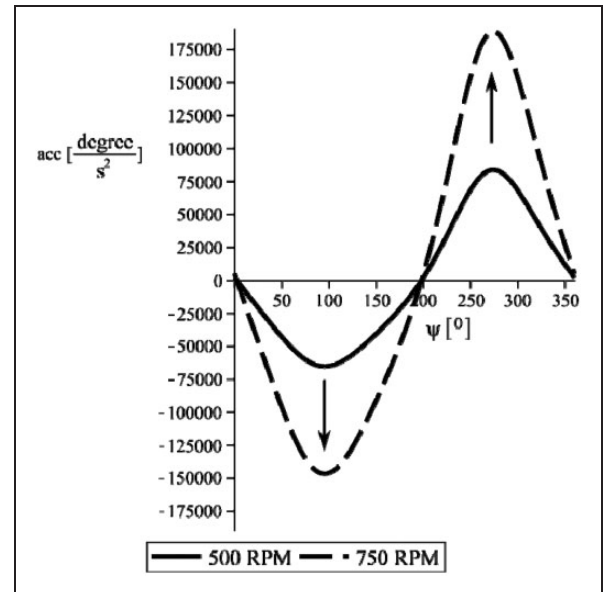


**Figure 9.** Rotational speed effect on angular acceleration curve for  $\varepsilon = 0^\circ$ .

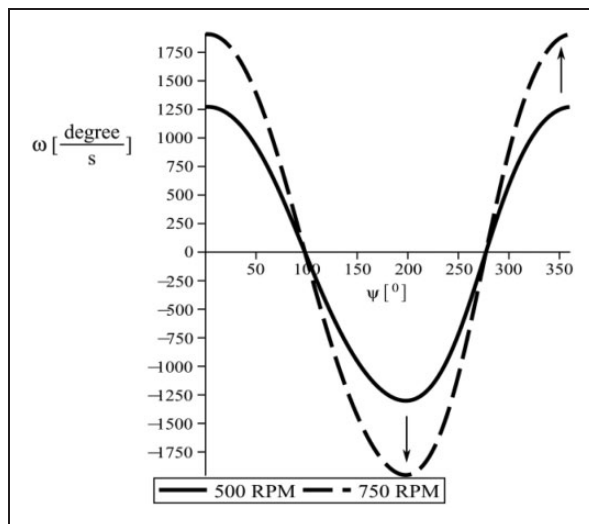


**Figure 8.** Rotational speed effect on angular velocity curve for  $\varepsilon = 0^\circ$ .

$$\text{acc} = \Omega^2 \cdot \frac{d^2\theta}{d\Psi^2} \quad (11)$$

Using the previous rotor definition, whose parameters are described in Table 1, it is now possible to apply the angular velocity and acceleration equations. Figures 8–11 show the effects of rotational speed and eccentricity phase angle on angular velocity and angular acceleration curves.

### The equivalent rotor model for parametric design of cycloidal rotors

The model description will be divided in two parts, a kinematic and a dynamic one. The first will be

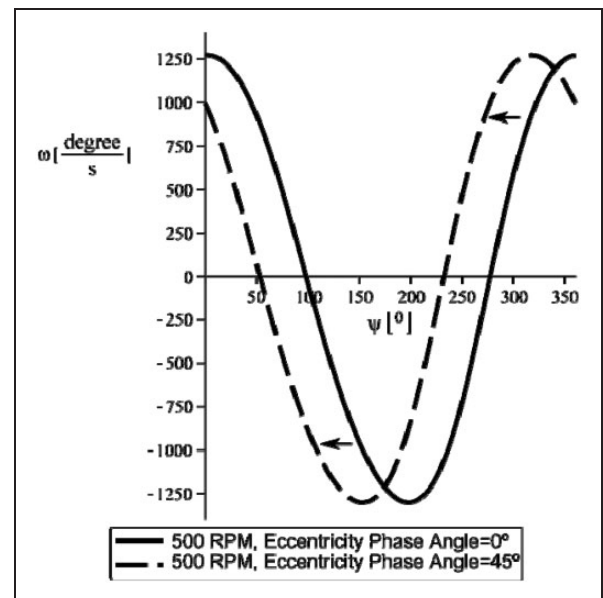


**Figure 10.** Effect of eccentricity phase angle on angular velocity curve.

important to identify the geometric feasibility of the rotor, in view of its complexity, the second will provide us with the forces, moments, and power obtained from the cyclorotor.

### Kinematic analysis

Considering that the rotor blades are represented by the chord, it is thus possible to create a mathematical relation which, depending on input parameters, generates a graphical representation of the geometry similar to a real rotor. In this case each blade slope is the

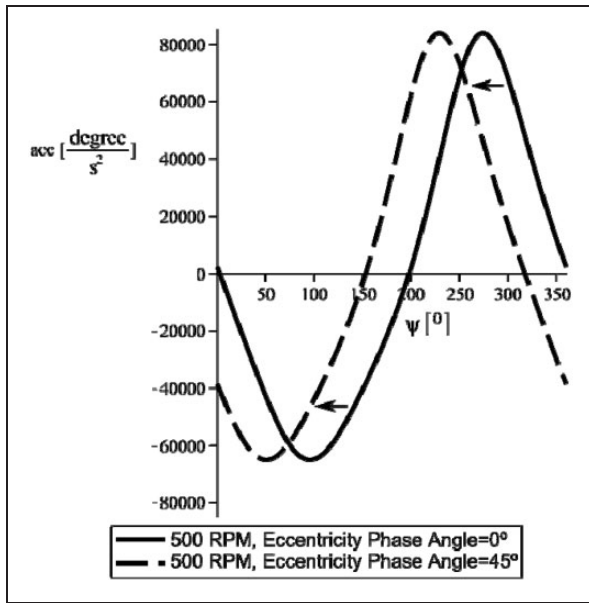


**Figure 11.** Effect of eccentricity phase angle on angular acceleration curve.

real inclination imposed by the dimensions of the considered mechanical control system. Using this function it was possible to study an animation of the cyclorotor blades. This part of the proposed analytical model is extremely useful, since it allows us to analyze many parameters, namely: the size of the blade chord relative to the cyclorotor's radius; to evaluate the position of the bearing point (pivot point) and its distance from the connection point of the control rod; to describe the distance between the blades; to define the eccentricity point; to describe the position of the blades according to the eccentricity phase angle; etc.

Equations (12), (13), (14), and (15) define the leading edge and trailing edge coordinates, see Figure 12. Their values can be obtained by introducing data from equations (4) and (5). Additionally it is necessary information on the eccentricity point, on the pivot point, also on the connection point of the control rod, and this can be obtained from their coordinates taking into account the data defined for the rotor under analysis, see Table 1. For the sake of brevity the mathematical expressions which compute all those information are not presented here. Figure 13 presents the results generated by the aforementioned equations taking as input parameters the rotor shown in Table 1. The considered eccentricity phase angle is  $45^\circ$ . Using Figure 13 the geometric interference between blades can be evaluated, also the ratio between chord and rotor diameter, as this latter is related to the degree of oscillation by the reduced frequency of oscillation. It can also be evaluated the distance between the pivot point and the connection point, i.e. if the chord is too short it may become impossible to have enough space to introduce the control rod. In this way, one can immediately

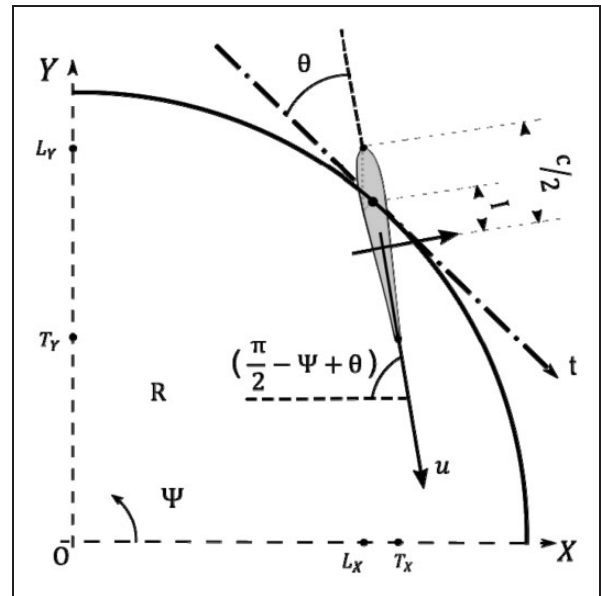


**Figure 12.** Real blades configuration.

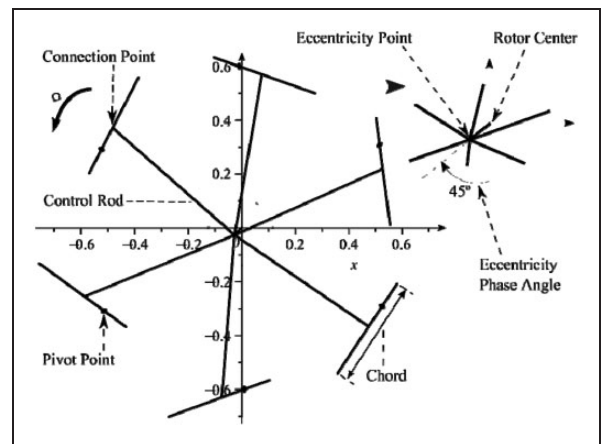


**Figure 13.** Real blades configuration,  $\varepsilon = 45^\circ$ .

analyze the operation of the cycloidal rotor, for a given set of data that defines the rotor dimensions. Figure 14 shows the change of blades pitch angle for an eccentricity of  $180^\circ$ .

$$L_X = R \cos(\Psi) - \left(\frac{1}{2}c + I\right) \cos\left(\frac{\pi}{2} - \Psi + \theta\right) \quad (12)$$

$$L_Y = R \sin(\Psi) + \left(\frac{1}{2}c + I\right) \sin\left(\frac{\pi}{2} - \Psi + \theta\right) \quad (13)$$

$$T_X = R \cos(\Psi) + \left(\frac{1}{2}c - I\right) \cos\left(\frac{\pi}{2} - \Psi + \theta\right) \quad (14)$$

$$T_Y = R \sin(\Psi) - \left(\frac{1}{2}c - I\right) \sin\left(\frac{\pi}{2} - \Psi + \theta\right) \quad (15)$$

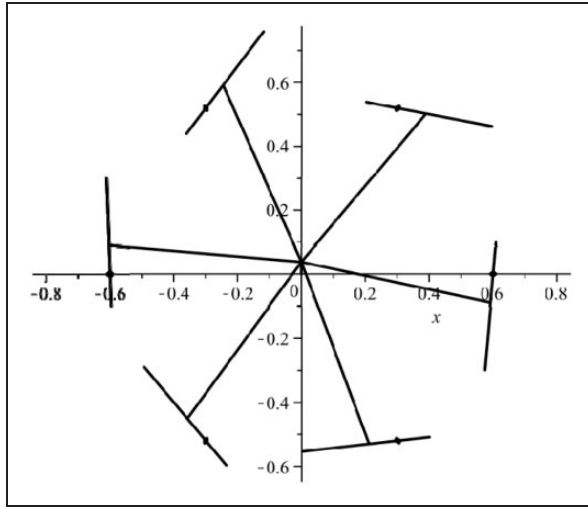


**Figure 14.** Real blades configuration,  $\varepsilon = 180^\circ$ .

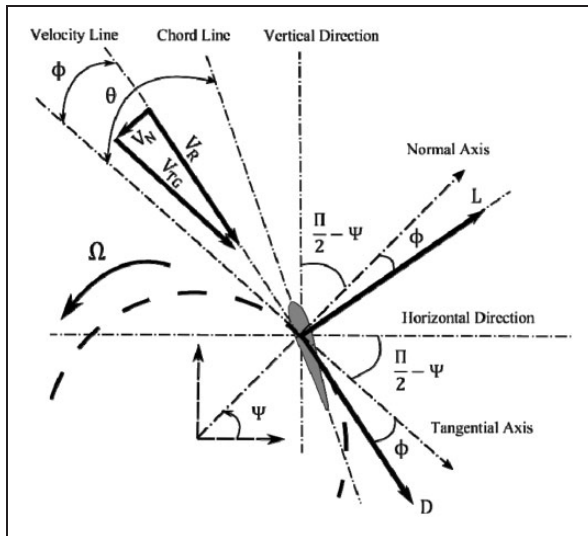


**Figure 15.** Horizontal and vertical components, for the resultant force, on a blade of cycloidal rotor in hovering state.

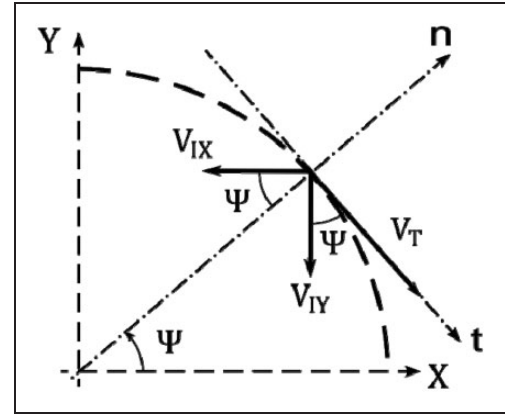
### Aerodynamic analysis

Figure 15 represents the dynamic forces applied to a cyclorotor blade in hovering state. The induced downwash angle is here associated with the existence of a resultant velocity whose normal component changes the angle of attack and, consequently, the lift and drag on each blade. By decomposing the lift and drag vectors, and using a trigonometric angular reduction to the first quadrant, the resultant forces in vertical and horizontal directions are defined by,

$$F_X = L \cos(\Psi - \phi) + D \sin(\Psi - \phi) \quad (16)$$

$$F_Y = L \sin(\Psi - \phi) - D \cos(\Psi - \phi) \quad (17)$$

The velocity vector can be decomposed in tangential and normal direction to define the induced angle



**Figure 16.** Analysis of induced velocities created by downwash.

by downwash phenomenon  $\phi = \tan^{-1}(V_N / V_{TG})$ . The tangential and normal components of the resultant velocity are  $V_R \cos \phi$  and  $V_R \sin \phi$ , respectively. Further, the tangential velocity due to the rotor rotational movement is  $V_T = \Omega R$ .

Alternatively, the resultant velocity can also be expressed through an analysis of the induced downwash velocities depicted in Figure 16. Here the downwash phenomenon is expressed in terms of induced velocities, in the vertical  $V_{IY}$  and horizontal  $V_{IX}$  directions, and not by induced angle as above.

Equations (18) and (19) show the resultant velocity in the tangential and normal direction.

$$V_{TG} = V_T - V_{IX} \sin(\Psi) + V_{IY} \cos(\Psi) \quad (18)$$

$$V_N = -V_{IX} \cos(\Psi) - V_{IY} \sin(\Psi) \quad (19)$$

Combining equations (18) and (19) with the previous expressions obtained for tangential and normal components, as a function of  $\phi$ , for the resultant velocity found from Figure 15, the induced velocities can now be expressed as,

$$V_{IX} = V_T \sin(\Psi) - V_R \sin(\Psi + \phi) \quad (20)$$

$$V_{IY} = V_R \cos(\Psi + \phi) - V_T \cos(\Psi) \quad (21)$$

Unsteady aerodynamics, supported on an analytical framework, is still nowadays a direct consequence of Theodorsen work on potential flow, for the lift and pitching moment, on a pitching and plunging thin blade/airfoil. That theory considers small perturbations and a harmonic motion. Since the function that Theodorsen found was solely dependent on reduced frequency it was concluded that this one was the correct way to consider the flow unsteadiness. Here it is used, instead, the Garrick<sup>30,31</sup> model, this author expanded the early work by presenting an equation for the propulsive force on a pitching thin airfoil. This model is obtained by balancing the conservation of energy, in order to compute the

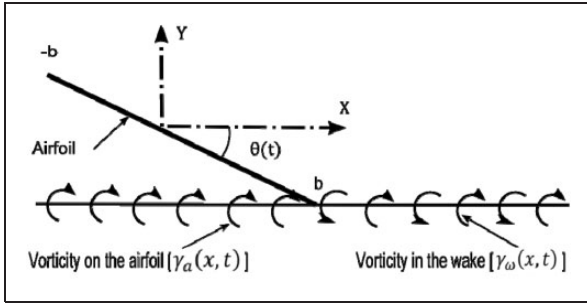


**Figure 17.** Vortex model pitching flat plate, adapted from Heerenbrink.<sup>32</sup>

propulsive energy as a function of structural energy and energy of the wake, and also by a direct computation of forces, with the propulsive force computed directly by calculating the leading edge suction on a thin airfoil.

Thus, Garrick model is used to take into account the effect of the blade oscillation in the cyclorotor model as it rotates. Apart from other differences, the Garrick model is used in McNabb<sup>30</sup> with resultant velocity and the induced angle of attack obtained through equations developed and proposed by McNabb.<sup>30</sup> In our model it is made assumptions concerning the direction and magnitude of resultant velocity vector. Equation (23) considers two-dimensional unsteady lift.  $F$  and  $G$  functions are standard Bessel functions of the first and second kinds, of argument  $k$ , which are components of initial Theodorsen's function used to express analytically the vorticity on the airfoil,  $\gamma_a(x, t)$ , represented in Figure 17, for an harmonically pitching flat plate<sup>32</sup> whose expression, under certain conditions, is represented by equation (22).

$$i\omega\hat{y}_a(x) + U_\infty \frac{\partial \hat{y}_a(x)}{\partial x} = -\frac{1}{2\pi} \int_{-b}^b \frac{\hat{\gamma}_a(\xi)}{x-\xi} d\xi + \frac{i\omega}{2\pi U_\infty} \hat{\Gamma} \int_b^\infty \frac{e^{i\omega(\frac{b-\xi}{U_\infty})}}{x-\xi} d\xi \quad (22)$$

$$\begin{aligned} \frac{L}{S} = & \rho b^2 (V_R \pi \omega - \pi b I \text{acc}) \\ & + C_{L\alpha 3D} \rho V_R b F \left[ V_R (\theta + \phi) + b \left( \frac{1}{2} - I \right) \omega \right] \\ & + \frac{C_{L\alpha 3D} \rho V_R b G}{\Omega} \left[ V_R \omega + b \left( \frac{1}{2} - I \right) \text{acc} \right] \end{aligned} \quad (23)$$

The 3-D lift curve slope of the airfoil is given by equation (24).<sup>33,34</sup> The variable  $\beta = \sqrt{1 - \text{Mach}}$  is the Prandtl-Glauert compressibility factor which in the present case is approximately equal to 1 since for a low pitch mechanical system the Mach number is negligible, that is to say, the tip speed of the blade is generally much less than the speed of sound. Figure 18 shows the sweep angle of an airfoil. As one can see

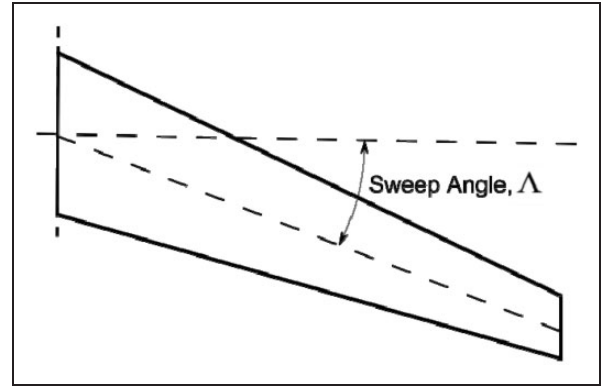


**Figure 18.** Airfoil sweep angle.

through Figure 1, the blades on the cyclorotor have no sweep angle. In this way, the equation for 3-D lift curve slope reduces to equation (25).

$$\frac{C_{L\alpha 3D}}{A_R} = \frac{2\pi}{2 + \sqrt{\frac{4\pi^2 A_R^2}{C_{L\alpha}^2} \left( 1 + \frac{\tan^2(\Lambda)}{\beta^2} \right)} + 4} \quad (24)$$

$$C_{L\alpha 3D} = \frac{2\pi A_R}{2 + \sqrt{\frac{A_R^2 4\pi^2}{C_{L\alpha}^2} + 4}} \quad (25)$$

### Semi-empirical approximation

The unsteadiness of the flow aerodynamic involves a number of unknown variables that exceeds the number of equations. Therefore, with the aim at simplifying the problem, the proposed model is based on several assumptions:

1. It is considered a cycloidal rotor assuming that the flow is *theoretically operating in steady aerodynamic conditions* with negligible downwash induced angle. Such rotor is “equivalent” to another cycloidal rotor, capable of producing the same amount of thrust and power, but operating in unsteady aerodynamic conditions.

In order to ensure steady aerodynamics it was considered the parameter used to describe the degree of unsteadiness. This parameter is the reduced frequency  $k$ . When it takes values less than or equal to 0.05, the unsteady effects may be neglected.<sup>24</sup> To consider this “equivalent rotor” assumption valid, in steady aerodynamics, it is required that the motion of the airfoil upwards, downwards, or in rotation, to be much slower than the time it takes for the air to travel from the leading edge to the trailing edge. Therefore, the resultant velocity for the “equivalent rotor”,  $V_{RS}$ , considering this steady aerodynamics, with no downwash, is computed using:

$$V_{RS} = \frac{k}{0.05} V_R \quad (26)$$



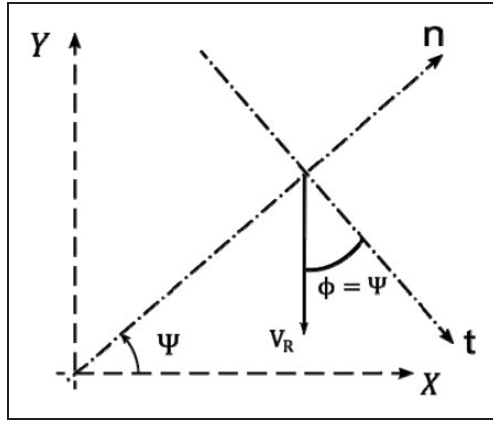


**Figure 19.** Induced angle analysis.

Actually, if the fluid moves sufficiently fast in a way that it does not feel the motion of the blade, the unsteady effects may be immediately neglected. In this way,  $V_{RS}$  increases as  $k$  increases. Note that the resultant velocity in a steady flow,  $V_{RS}$ , is always higher than the resultant velocity in the unsteady situation,  $V_R$ , because  $k$  is always greater than 0.05. Actually, if  $k$  is not greater than 0.05 there is no purpose to determine the “equivalent rotor” because the real rotor is already in steady aerodynamics condition.

2. It is assumed that the flow in each blade is deflected vertically downwards,  $\phi = \Psi$ .

It was assumed that in the unsteady aerodynamic situation, with downwash, the fluid is deflected vertically downwards. Blades produce lift by forcing the air to flow downwards and the reaction force pushes the propeller upwards. Since it is considered a hovering state, the reaction should be essentially vertical aiming to cancel the weight of the system. The induced angle  $\phi$  is the angle between resultant velocity and the tangent line, see Figure 15. It is clear by the geometric analysis of Figure 19 that  $\phi$  coincides with the azimuthal angle.

3. Finally it is assumed that in all azimuthal positions the resultant velocity  $V_R$  is lower than  $\Omega R$ . This velocity will be scaled using an empirical parameter.

It is known that there are azimuthal positions where the resultant velocity is higher than  $\Omega R$  and others where the velocity is lower. Actually, these values depend on the induced velocity vector. In our model, it was assumed a resultant velocity at each blade lower than  $\Omega R$  because it is known that the blades do not contribute equally to the production of thrust. Certain positions of the azimuth angle correspond to a very low angle of attack and consequently the blades at these azimuthal positions hardly contribute to the generation of thrust. Thus, our analysis is based on the overall contribution from all the blades and not on the individual blade, because the flow around the individual blade is quite complex and impossible to be predicted analytically. An

example of this complexity is the variation of the aerodynamic center along the chord as the blade changes its azimuthal position. Further, for the real case the reaction on the blades is not exactly vertical as well. The blades do not perfectly contribute to the generation of thrust. Thus, in the context that the fluid is deflected vertically downward, it was considered the reduction of resultant velocity as a way to compensate for the perfect vertical deflection as above assumed. Therefore, within the context of our analysis, the resultant velocity in the unsteady situation,  $V_R$  is scaled through an empirical parameter  $E$ ,

$$V_R = \frac{\Omega R}{E}, \quad E > 1 \quad (27)$$

To define the value of  $E$  the experimental report of Bosch was considered.<sup>30,35</sup> Their results have confirmed that force and power do not vary linearly with the rotating speed, thrust varies with the square of RPM and the power varies with the cube. Here the analytical model is correlated with the force rate, thus a linear function for  $E$  vs  $V$  was devised. Albeit this approximation, this approach is adequate for establishing a fast preliminary design model, as was shown in the results obtained in “Analytical model results” section. This linear function can easily be defined by its slope and y-axis intercept. Although different rotors exhibit different values of force and power, their curves have similar shape, that is to say, their values grow at an increasing rate. Thus, it was assumed that the gradient of function  $E$  has always the same shape for all different future rotors in analysis. In order to find this common function experimental data from Bosch rotor was used.<sup>30,35</sup> By using these values it was possible to determine a generic expression for  $E$  that should also work for other rotors,

$$E = -\frac{3}{10300}\Omega + \frac{p}{10300}(5688.6e^{-0.062p} + E_1) \quad (28)$$

$$E_1 = 8.33(32.5p - 1042.85)\sigma - 97.5p + 3048.55. \quad (29)$$

Generally, the maximum and minimum pitch angles are symmetric. However, it is perfectly possible to consider rotor cases with asymmetric pitching and for those the average value of the difference between the maximum and the minimum pitch angle  $p$  can be considered. In order to verify its generality, the equation was tested using data from alternative rotors.<sup>22,36</sup> These rotors are different in size and maximum pitch angle from the first rotor that was used to determine equation (28).

Figure 20 shows a slope value of  $E$  at different pitching conditions as a function of rotating speed. It can be observed that the linear function decreases as the rotational speed increases. Thus, the model can

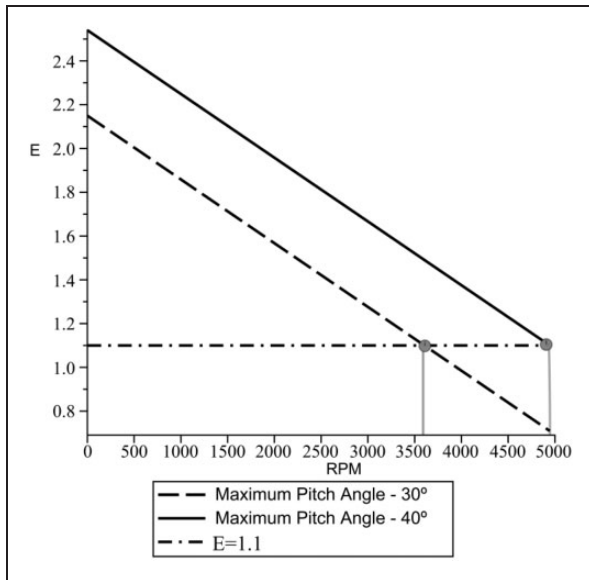


**Figure 20.** Verification of the generality of the  $E$  function concept.

be applied only up to a certain value of the rotational speed, being that imposed by the pitch angle and the condition  $E > 1$ . Assuming  $E = 1.1$  as the minimum value, the maximum rotational speeds that can be considered are 3604.5 r/min and 4945.2 r/min for rotors whose maximum pitch angle are  $30^\circ$  and  $40^\circ$ , respectively. These features are readily seen in Figure 20, assuming solidity equal to 0.48.

Further, if one is interested in determining the maximum and minimum pitch angle, they can be obtained by computing the derivative of equation (4).

For the “equivalent rotor” theoretically in steady aerodynamic situation, the resultant velocity  $V_{RS}$  is tangential and there is no induced angle of attack. Thus, equations (16) and (17) revert into,

$$F_X = L \cos(\Psi) + D \sin(\Psi) \quad (30)$$

$$F_Y = L \sin(\Psi) - D \cos(\Psi) \quad (31)$$

The calculation of moment  $M$  and power  $P$  is made by using equations (32) and (33).

$$M = \sum_{i=1}^N (F_{Yi} R \cos(\Psi_i) + F_{Xi} R \sin(\Psi_i)) \quad (32)$$

$$P = M\Omega \quad (33)$$

The entire proposed model is described in detail by the flowchart in Figure 21. The numbers within the rectangles indicate the sequence of calculations. They are described below:

1. Input of rotor parameter  $R, l, d, e, S, c, I, \Omega, \varepsilon$ .
2. Calculation of pitch angle,  $\theta$ , using equation (4).

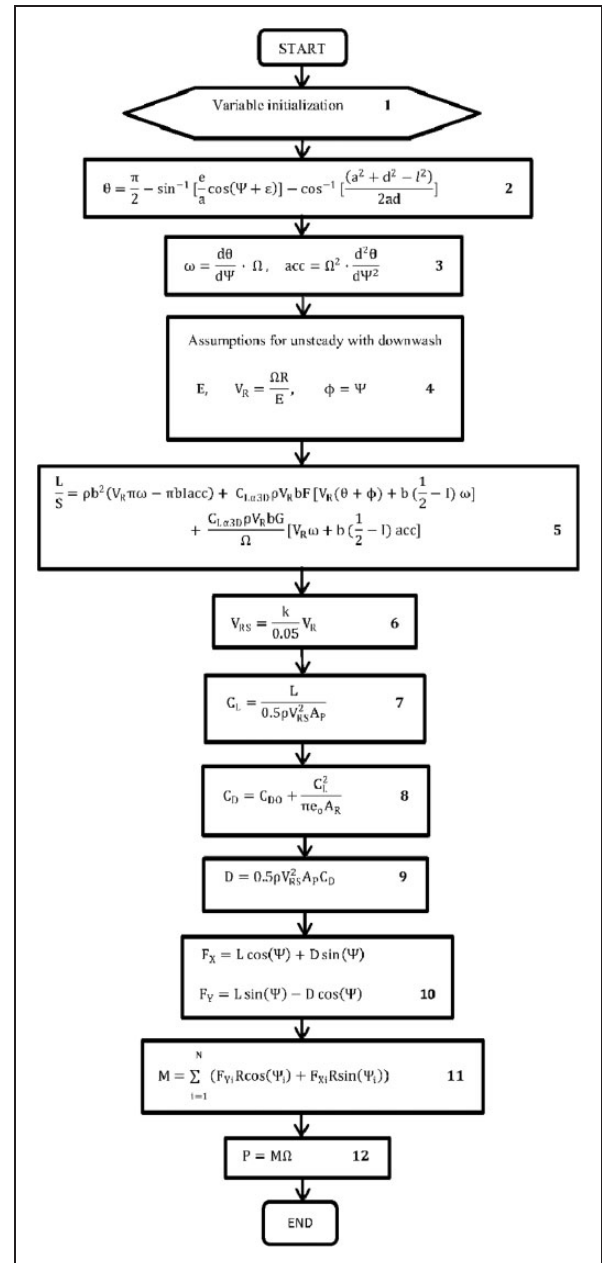


**Figure 21.** Description of the proposed model.

3. Calculation of angular velocity,  $\omega$ , and angular acceleration  $acc$ .
4. Calculation of empirical parameter  $E$  (equation 28) in order to obtain a scaled velocity  $V_R$  (equation 27). Assumption that the flow is vertically deflected by the blade ( $\phi = \Psi$ ).
5. Calculation of lift,  $L$ , using an unsteady aerodynamic approximation, equation (23).
6. Calculation of resultant velocity,  $V_{RS}$  (equation 26) for the “equivalent rotor” operating in steady aerodynamics.
7.  $C_L$  calculation for the “equivalent rotor”, so that the blades produce the same lift as the unsteady rotor.
8. Calculation of drag coefficient  $C_D$ .
9. Drag force calculation,  $D$ .

10. Decomposition of forces on their vertical and horizontal directions, neglecting the downwash induced angle.
11. Calculation of binary.
12. Calculation of power.

It is known that in the present case, i.e. case of cyclorotor, the profile drag coefficient has a strong dependence on Reynolds number<sup>21</sup> and its value should take into account the effect of flow curvature.<sup>13</sup> Since the present work is purely analytic, to assess its approximate value, it was considered experimental data previously used to determine function  $E$ . Thus, the value found was 0.043.

### Analytical model results

The results obtained by using the new analytic model were compared with data from experimental testing, as shown in Figures 22–27. To this end, data from Bosch Aerospace,<sup>30,35</sup> Seoul National University,<sup>22</sup> and IAT21<sup>36</sup> were considered. Tables 2–4 contain the parameters that allow us to define the rotor and mechanical pitching control system dimensions.

Considering the Bosch test case results that are shown in Figures 22 and 23 it can be seen that,

although the deviations increase for lower rotating speeds, they are approximately the same for the thrust and power. This does not happen in the IAT 21 and Seoul test cases, see Figures 24–27. Such behavior can be explained by the fact that function  $E$  was determined through the Bosch. Figure 26 shows a good agreement between the analytical values and the experimental results. This good matching may be

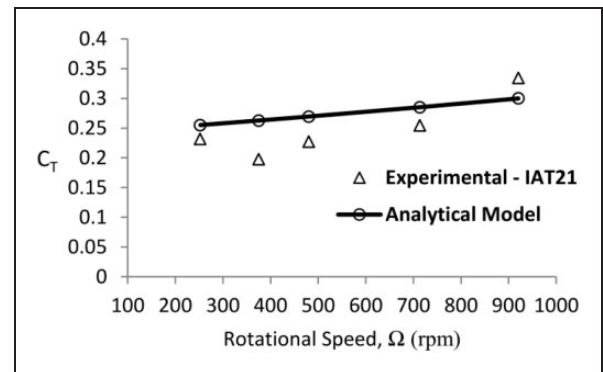


**Figure 24.** Thrust coefficient as a function of rotor angular velocity, comparison between experimental and analytic results—IAT21 case.<sup>36</sup>

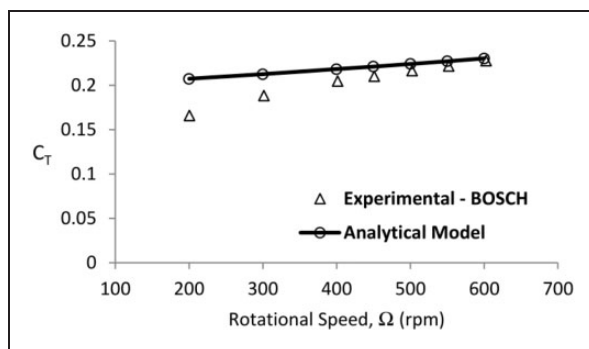


**Figure 22.** Thrust coefficient as a function of rotor angular velocity, comparison between experimental and analytic results, Bosch case.<sup>30,35</sup>

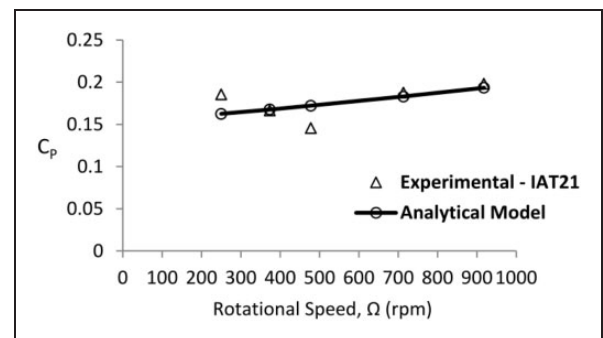


**Figure 25.** Power coefficient as a function of rotor angular velocity, experimental, and analytic results—IAT21 case.<sup>36</sup>

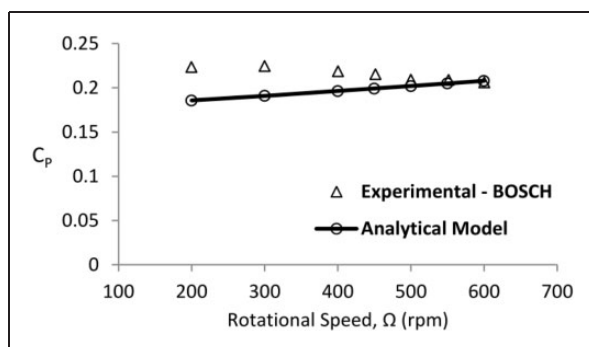


**Figure 23.** Power coefficient as a function of rotor angular velocity, comparison between experimental and analytic results, Bosch case.<sup>30,35</sup>

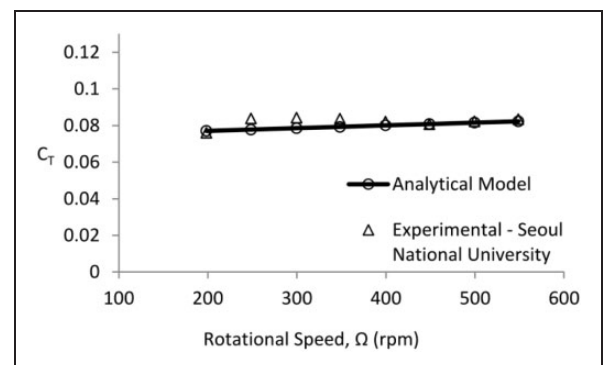


**Figure 26.** Thrust coefficient as a function of rotor angular velocity, experimental, and analytic results—Seoul National University case.<sup>22</sup>

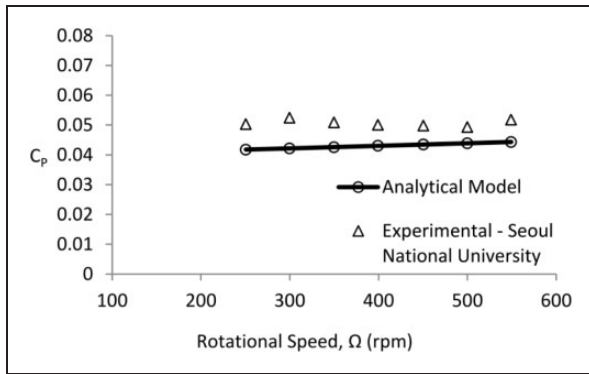


**Figure 27.** Power coefficient as a function of rotor angular velocity, experimental, and analytic results—Seoul National University case.<sup>22</sup>

**Table 2.** Definition of cyclorotor parameters—Bosch case.<sup>30,35</sup>

Variable	Value
Airfoil	NACA 0012
Rotor diameter (m)	1.2192
Span (m)	1.2192
Chord (m)	0.3048
Pitching axis location (m)	25% of chord
Number of blades	6
Length of control rod (m)	0.6134
Magnitude of eccentricity (m)	0.0315
Phase angle of eccentricity ( $^\circ$ )	0
$d$ (m)	0.075
Maximum and minimum pitch angle ( $^\circ$ )	25; -25

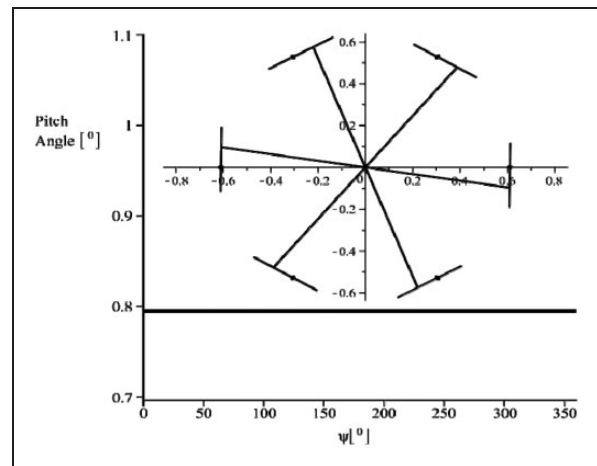
**Table 3.** Definition of cyclorotor parameters—IAT21 case.<sup>36</sup>

Variable	Value
Airfoil	NACA 0016
Rotor diameter (m)	1.2
Span (m)	1.2
Chord (m)	0.3
Pitching axis location (m)	35% of chord
Number of blades	6
Length of control rod (m)	0.61
Magnitude of eccentricity (m)	0.072
Phase angle of eccentricity ( $^\circ$ )	0
$d$ (m)	0.12
Maximum and minimum pitch angle ( $^\circ$ )	36.1; -39.1

related to the blade interference effects which in this case are less intense because the ratio  $c/R$  is not high. Another reason is that the blades are operating at lower pitch angle and this may correspond to the reduction of the unsteadiness effects. Thus, in the

**Table 4.** Definition of cyclorotor parameters—Seoul National University case.<sup>22</sup>

Variable	Value
Airfoil	NACA 0012
Rotor diameter (m)	0.8
Span (m)	0.8
Chord (m)	0.15
Pitching axis location (m)	25% of chord
Number of blades	6
Length of control rod (m)	0.4038
Magnitude of eccentricity (m)	0.05 R
Phase angle of eccentricity ( $^\circ$ )	10
$d$ (m)	0.059
Maximum and minimum pitch angle ( $^\circ$ )	20; -20



case of IAT 21, Figure 24, in which the blade reaches a pitch angle of approximately  $40^\circ$ , the deviation increases to 12.8%. On the other hand, the deviation concerning the power in Figure 27 is larger than that corresponding to the thrust. This occurrence may be related to the assumption considered and the adjustment of  $C_{DO}$  value. It is known that the  $C_{DO}$  value is not constant. However, in the proposed model the  $C_{DO}$  value that was obtained by using the experimental results from Bosch is kept constant even for the others rotors. The growth of the predicted thrust and power coefficients is observed through the obtained results in Figures 22–27. One of the reasons that led us to consider the function  $E$  obtained from Bosch experimentally tested rotor is the inclusion of aspects which have been impossible to model analytically in the present study due to the associated complexities. As examples it may be pointed the aeroelastic effects and the variation of the aerodynamic center along the chord as the blade change its azimuthal position.

The three rotors were also considered in a special working condition for which the magnitude of



eccentricity is equal to zero. In this particular situation the pitch angle becomes constant and the thrust generated, predicted by the analytical model, is always zero. This result is similar to the one presented in Nakaie et al.<sup>25</sup> In both results, analytic and experimental, the power is not zero, because the rotor must overcome the profile drag, even if not providing thrust. For this case, Figure 28 shows the pitch angle and the blades' configuration, for zero thrust, predicted by our analytical model using Bosch rotor geometry definition. The pitch angle, identified by the horizontal line in Figure 28, is 0.795.

## Conclusions

The proposed "equivalent rotor" analytical model allows to study the operation of a cyclorotor in hovering state. It assumes a real blade motion and unsteady aerodynamics with downwash phenomenon. The model was used to study the cyclorotor blades motion in terms of their positioning, and on the operation of the kinematic control rod system. This allowed detecting which dimensions, for the several parameters of the system, render a viable working rotor, i.e. control pitching mechanism without interference and producing thrust for a defined maximum pitching angle. Using the proposed analytical tool it was possible to define a set of conclusions that can be stated as:

1. The motion of the blades imposed by the pitch mechanical control system may lead to a non-perfect cycloid, or to a pure cycloidal motion. This information is important to be taken into account during the construction of the rotor, since it is important for the aircraft control.
2. It was verified, through the performed simulations, that the maximum pitch angle may be increased by increasing the magnitude of the eccentricity. Note that the increase of eccentricity causes a deviation of the steering point zone to out of the circle described by the rotor. In other words, from a certain eccentricity value, the motion of blades requires a sinusoidal high pitch mechanical system.
3. The maximum and minimum values of angular velocity, and acceleration, are imposed by the rotational speed. However, the azimuthal angles where these values occur are a direct consequence from the eccentricity phase angle.
4. The comparison of our model with experimental data from Bosch, IAT 21 and Seoul National University rotors showed that the deviation of the computed forces to be 4.8%, 12.8%, and 1.6%, respectively. Concerning power, the shift from experiments was found to be 4.2% for the Bosch test case, 3.4% for the IAT 21 rotor, and 8% for the Seoul National University configuration.

The present "equivalent rotor" analytical model, albeit not allowing to study in detail the flow field, like CFD, is still a very important tool in the preliminary design of cyclorotors. Further, it is of paramount importance to help define the control in lift and thrust forces, when operating a cyclorotor based air-vehicle.

## Conflict of interest

None declared.

## Funding

The present work was performed as part of Project CROP, supported by European Union within the 7th Framework Programme under grant number 323047, and also supported by C-MAST, Centre for Mechanical and Aerospace Science and Technology Research Unit No. 151.

## References

1. Yun CY, Park IK, Hwang IS, et al. Thrust control mechanism of VTOL UAV cyclocopter with cycloidal blades system. *J Intell Mater Syst Structures* 2005; 16: 937–943.
2. Wang X and Lin H. Design and control for rotor-fixed wing hybrid aircraft. *Proc IMechE, Part G: J Aerospace Engineering* 2011; 225(7): 831–847.
3. Lopez-Garcia O, Cuerva A and Esteban S. Use of calculus of variations to determine the shape of hovering rotors of minimum power and its application to micro air vehicles. *Proc IMechE, Part G: J Aerospace Engineering* 2012; 226(5): 574–588.
4. Tanaka K, Suzuki R, Emaru T, et al. Development of cyclogyro-based flying robot with variable attack angle mechanisms. *IEEE/ASME Trans Mechatron* 2007; 12(5): 565–570.
5. Boschma JH. *BRI cyclo-turbine for energy production*. Brownsboro, AL: Boschma Research, Inc, 2011.
6. Kirsten F. Cycloidal propulsion applied to aircraft. *Trans Am Soc Mech Eng* 1928; 50: AER-50-12.
7. Gibbens RP and Boschma JH. Construction and testing of a new aircraft cycloidal propeller. In: *13th AIAA lighter-than-air systems technology conference*, Norfolk, VA, AIAA No. 99-3906, 1999, pp.1–9.
8. Martinez-Val R, Perez E, Puertas J, et al. Optimization of planform and cruise conditions of a transport flying wing. *Proc IMechE, Part G: J Aerospace Engineering* 2010; 224(12): 1243–1251.
9. Boschma JH. Modern aviation applications for cycloidal propulsion. In: *AIAA Aircraft Technology Integration and Operations Forum*, 2001.
10. Iosilevskii G and Levy Y. Experimental and numerical study of cyclogiro aerodynamics. *AIAA J* 2006; 44(12): 2866–2870.
11. Hu Y, Lim KB and Hu WR. The research on the performance of cyclogiro. In: *6th AIAA aviation technology, integration and operations conference*, Wichita, Kansas, 25–27 September 2006.
12. Benedict M, Ramasamy M and Chopra I. Improving the aerodynamic performance of micro-air-vehicle-scale cycloidal rotor: an experimental approach. *J Aircraft* 2010; 47(4): 1117–1125.

13. Benedict M, Jarugumilli T and Chopra I. Effect of rotor geometry and blade kinematics on cycloidal rotor hover performance. *J Aircraft* 2013; 50(5): 1340–1352.
14. Páscoa JC and llieva GI. Overcoming stopovers in cycloidal rotor propulsion integration on air vehicles. In: *Proceedings of the ASME 2012 international design engineering technical conferences & computers and information in engineering conference*, Chicago, IL, IDETC/CIE, 12–15 August 2012.
15. Lee CH, Min SY, Kim YS, et al. Design of two-rotored UAV cyclocopter. In: *5th European Conference for Aeronautics and Space Sciences*, Munich, Germany, 1–5 July 2013, Korea Aerospace Research Institute.
16. Benedict M, Chopra I, Ramasamy M, et al. Experimental investigation of the cycloidal rotor for a hovering micro air vehicle. In: *Proceedings of the 64th annual national forum of the American Helicopter Society*, Montreal, Canada, 28–30 April 2008.
17. Hwang IS, Min SY, Kim MK, et al. Multidisciplinary optimal design of cyclocopter blade system. In: *46th AIAA/ASME/ASCE/AHS/ASC structures, structural dynamics, and materials conference*, AIAA 2005-2287, Austin, TX, 2005.
18. Boirum CG and Post SY. Review of historic and modern cyclogiro design. In: *45th AIAA/ASME/SAE/ASEE joint propulsion conference & exhibit*, AIAA 2009-5023, 2009.
19. Hwang IS, Min SY, Lee CH, et al. Development of a four-rotor cyclocopter. *J Aircraft* 2008; 45(6): 2151–2157.
20. Yu H, Fan D, Gang W, et al. Two dimensional numerical simulation of cycloidal propellers with flat plate airfoil in hovering status. In: *AIAA international powered lift conference*, Los Angeles, California, 12–14 August 2013.
21. Benedict M, Mataboni M, Chopra I, et al. Aeroelastic analysis of a micro-air-vehicle-scale cycloidal rotor in hover. *AIAA J* 2011; 49(11): 2430–2443.
22. Yun CY, Park IK, Lee HY, et al. *A new VTOL UAV cyclocopter with cycloidal blades system*. American Helicopter Society International, June 2004.
23. Kim SJ, Yum CY, Kim D, et al. Design and performance tests of cycloidal propulsion systems. In: *44th AIAA/ASME/ASCE/AHS structures, structural dynamics, and materials conference*, AIAA 2003-1786, Norfolk, VA, 2003.
24. Parsons ES. *Investigation and characterization of a cycloidal rotor for application to a micro-air vehicle*. Master Thesis, Department of Aerospace Engineering, October 2005.
25. Nakaie Y, Ohta Y and Hishida K. Flow measurement around a cycloidal propeller. *J Vis Soc* 2010; 13: 303–310.
26. Nakonechny BV. Experimental performance of a six-bladed vertical axis propeller. Report No. 1446, Department of the Navy, January 1961.
27. Foshag WF and Boehler GD. Review and preliminary evaluation of lifting horizontal—axis rotating-wing aeronautical systems (HARWAS). *USAAVLABS Technical Report*, Fort Eustis, Virginia, March 1969, vol. 69, no. 13.
28. Manen Jv and Terwisga Tv. A new way of simulating whale tail propulsion. In: *Twenty-first symposium on naval hydrodynamics*, 1997.
29. Bartels J and Jürgens D. *The Voith Schneider propeller current applications and new developments*. G 1849 e Print Run 1500 aK/Wo Printed in German, December 2006.
30. McNabb ML. *Development of a cycloidal propulsion computer model and comparison with experiment*. Master Thesis, Faculty of Mississippi State University, December 2001.
31. Garrick IE. *Propulsion of a flapping and oscillating airfoil*. NACA Report No. 567, 1936, pp.419–427.
32. Heerenbrink MK. Simultaneous PIV and balance measurements on pitching aerofoil. Master of Science Thesis, Delft University of Technology, 30 May 2011.
33. Raymer DP. *Aircraft design: a conceptual approach*. American Institute of Aeronautics and Astronautics, Inc., Washington, DC, 1989.
34. Etkin B and Reid LD. *Dynamics of flight: stability and control*. 3rd ed. Canada: John Wiley & Sons, Inc, 1996.
35. Boschma JH. *Cycloidal propulsion for UAV VTOL applications*. SBIR Topic Number N98-022, Bosch Aerospace, Inc, November 1998.
36. Xisto CM, Páscoa J, Abdollahzadeh M, et al. PECyT-plasma enhanced cycloidal thruster. In: *50th AIAA/ASME/SAE/ASEE joint propulsion conference*, AIAA Paper 1946111, 2014, pp.8.

## Appendix

### Notation

$a$	distance from the pivot point to eccentricity point, m
$\text{acc}$	angular acceleration around pivot point, $\text{rad/s}^2$
$A$	pivot point
$A_P$	projected area, $S.c$ , $\text{m}^2$
$A_R$	aspect ratio of the blade, $S^2/A_P$
$b$	semi chord of airfoil, m
$B$	steering center
$c$	chord of airfoil, m
$C_D$	drag coefficient, $C_{D0} + C_L^2/\pi e_o A_R$
$C_L$	lift coefficient, $L/0.5\rho V_{RS}^2 A_P$
$C_{D0}$	parasite drag coefficient
$C_{L\alpha 3D}$	3-D lift curve slope of the airfoil
$C_{L\alpha}$	2-D lift curve slope of the airfoil
$C_P$	power coefficient, $P/2\rho SR(\Omega R)^3$
$C_T$	thrust coefficient, $T/2\rho SR(\Omega R)^2$
$d$	distance from the pivot point to the connection point, m
$D$	drag force, $0.5\rho V_{RS}^2 A_P C_D$ , N
$e$	magnitude of eccentricity, m
$ep$	eccentricity point
$e_o$	Oswald factor, 0.26
$E$	eccentricity phase angle, deg
$F_X$	rotor horizontal force, N
$F_Y$	rotor vertical force, N
$I$	pivot point position measured on $u$ axis, m
$k$	reduced frequency of blade oscillation, $c/2R$
$l$	length of the control rod, m

$L$	2-D unsteady lift, N	$\overrightarrow{TA}$	tangent vector at each azimuthal position
$L_X$	X coordinate of leading edge		
$L_Y$	Y coordinate of leading edge		
$O$	rotor center	$\varepsilon$	eccentricity phase angle, deg
$P$	power, W	$\theta$	pitch angle, deg
$\overrightarrow{PA}$	pitch vector for steering center case	$\rho$	density of air, kg/m <sup>3</sup>
$r$	distance between steering center and rotor center, m	$\sigma$	rotor solidity, $Nc/2\pi R$
$R$	rotor radius, m		induced angle of attack, deg
$S$	span of airfoil, m	$\Psi$	azimuth angle, deg
$T$	thrust, $(F_X^2 + F_Y^2)^{0.5}$ , N	$\Psi_i(0)$	initial position of each blade, deg
$T_X$	X coordinate of trailing edge	$\Psi_r$	steering center position, deg
$T_Y$	Y coordinate of trailing edge	$\omega$	angular velocity around pivot point, rad/s
			rotational speed of rotor, rad/s